PHOTONICS Research

Directional broadband resonant fluorescence from Si bullseye resonators on a SiO_2/Au heterostructure

Yuheng Mao,[1,†] Lin Cai,[1,†] Lidan Zhou,[2,†] Mingcheng Panmai,[3] Shimei Liu,[4] Zhuo Wang,[1,5] and Sheng Lan[1,6]

[1]Guangdong Provincial Key Laboratory of Nanophotonic Functional Materials and Devices, School of Optoelectronic Science and Engineering, South China Normal University, Guangzhou 510006, China
[2]State Key Laboratory of Optoelectronic Materials and Technologies, School of Electronics and Information Technology, Sun Yat-sen University, Guangzhou 510006, China
[3]School of Electrical and Electronic Engineering, Nanyang Technological University, Singapore 639798, Singapore
[4]School of Physics and Optoelectronic Engineering, Foshan University, Foshan 528000, China
[5]e-mail: zhuowang@m.scnu.edu.cn
[6]e-mail: slan@scnu.edu.cn
[†]These authors contributed equally to this work.

Received 1 September 2025; revised 4 December 2025; accepted 22 December 2025; posted 24 December 2025 (Doc. ID 577859); published 24 March 2026

Silicon (Si) based light emitters compatible with standard CMOS fabrication are critical for integrated photonics, yet conventional Si nanoparticles suffer from severe dissipation losses under high-density carrier injection that limit directional hot electron luminescence when they act as light sources. Resolving this limitation, we developed optimized Si bullseye resonators on a silica/gold heterostructure substrate that enable broadband directional luminescence through the resonant mechanism of the Bragg gratings. First, the central Si nanopillar is designed for sustaining strong magnetic dipole and mirror-image-induced magnetic dipole resonances, enhancing two-photon absorption photoluminescence (PL) under the excitation of femtosecond laser pulses. Second, laterally propagating surface plasmon polaritons induced by the central nanopillar light source undergo efficient out-coupling via Bragg gratings, generating distinct emitted spectral peaks. Comparative collection efficiency measurements reveal that more than 60% of emitted energy across 470–600 nm is captured within a 29° half-aperture angle using a 0.7 NA oil-immersion objective. Notably, a dominant emission peak covering the 570–590 nm wavelength band concentrates 85% of energy within this angular range. The bullseye resonator concurrently amplifies Si PL at both excitation and emission stages while delivering pronounced mode selectivity and broadband collimation. This work establishes a practical pathway toward CMOS-compatible compact Si light sources.

https://doi.org/10.1364/PRJ.577859

1. INTRODUCTION

Silicon (Si) based light emitters compatible with the current fabrication technology of Si chips are highly desirable in integrated optical circuits [1,2]. Recently, Si nanoparticles with diameters in the range from 150 to 250 nm have attracted great interest because they support Mie resonances in the visible to the near-infrared spectral range, which can be employed to generate strong subwavelength-scale light enhancement and boost their nonlinear optical responses [3,4]. It has been demonstrated that the quantum efficiency of such a Si nanoparticle can be significantly enhanced by several orders of magnitude through injecting high-density carriers into the Si nanoparticle [5]. The carrier dynamics can be dramatically modified by exploiting the Auger recombination process and the intrinsic excitation of carriers induced by the high temperature, leading to highly efficient white light emission from the Si nanoparticle [6]. Specifically, under resonant excitation conditions, the hot electron luminescence intensity per unit of excitation energy is significantly enhanced in Si nanoparticles, laying the foundation for advanced Si-based light sources.

In previous studies, the focus was on constructing optical resonances at excitation wavelengths to generate high-density carriers in Si through enhanced two-photon or three-photon absorption (2PA or 3PA). Such optical resonances include conventional Mie resonances supported by a Si nanoparticle [7–9], supercavity modes [6,10], and quasi-bound states in the

continuum supported by a silicon/gold (Si/Au) hybrid metasurface [11–14]. The strong optical field confinement enabled by high-quality-factor (high-Q) resonances significantly lowers the excitation threshold needed for luminescence burst and greatly amplifies the emission intensity. However, after injecting high-density carriers, the dissipation loss in the Si nanoparticles will increase sharply [15], making it difficult to form a strong Purcell effect for radiation enhancement and emission direction manipulation. Consequently, the hot electron luminescence from a Si nanoparticle generally appears as white light. To achieve luminescence enhancement, in addition to adopting a Si nanoparticle as the optically active material, a resonant cavity that is not affected by carrier injection needs to be configured for it.

Currently, surface-emitting light sources based on resonant structures have attracted widespread attention, including vertical cavity surface emitters [16], photonic crystal surface emitters [17], and bullseye resonators [18]. Compared to in-plane emitters, surface-emitting devices offer the advantage of enabling high-density two-dimensional arrays and three-dimensional integration [19]. Among these structures, the bullseye resonator, characterized by its high Q/V_{eff} (where V_{eff} is the modal volume), stands as a strong candidate for realizing low-threshold light sources. For example, through coupling surface plasmon polaritons (SPPs) with the Bragg gratings, one can achieve unidirectional bright spontaneous emission [20] and radially polarized single photon generation [21]. In addition, waveguide modes in a high-index GaN thin film can interact with Bragg gratings fabricated via partial trench etching on the film surface, achieving high-efficiency broadband conversion to out-of-plane radiation modes [22]. Such a nonlocal coupling mechanism exhibits high sensitivity to grating periodicity while remaining robust against variations in the central active material, making it a well-suited architecture for enhancing fluorescence emission from Si nanoparticles. Moreover, under the Bragg resonance conditions, periodic ridge reflections boost the optical field intensity at the core region of a bullseye, generating pronounced enhancements in nonlinear optical phenomena [23,24]. However, existing approaches have been limited to enhancing only one stage, either excitation or emission, within a single device. The concurrent enhancement of both processes using one bullseye structure has not yet been demonstrated. It is therefore necessary to explore the enhancement effect of dual-band resonance based on a bullseye structure on photoluminescence in silicon.

In this article, we designed and optimized Si bullseye resonators on a silica/gold (SiO_2/Au) heterostructure substrate capable of broadband directional enhanced hot electron luminescence, fabricated using established Si chip fabrication processes. The central Si nanopillar in a bullseye resonator sustains strong magnetic dipole (MD) [25] and mirror-induced magnetic dipole (MMD) [26,27] resonances. This optical field concentration can be further boosted by enhanced backscattering from the circular Bragg grating. Simulations and experiments confirmed that the resonator significantly enhances excitation efficiency for 2PA photoluminescence (PL) in the Si nanopillar under 726 nm femtosecond laser excitation. In the meantime, the laterally propagating SPP modes induced by the central nanopillar light source can be efficiently coupled out by the Bragg gratings based on the second-order Bragg condition, manifesting as several peaks in the radiation spectrum. A comparative measurement of collection efficiencies between 1.3 NA and 0.7 NA oil-immersion objectives revealed that the 0.7 NA one can capture more than 60% of the emitted energy across the 470–600 nm spectral band. Moreover, a distinct emission peak was observed covering the 570–590 nm wavelength band, with 85% of the energy concentrated within a half-aperture angle of 29°. The findings established the bullseye architecture as a powerful platform that concurrently amplifies Si PL efficiencies at both excitation and emission stages, while exhibiting pronounced mode selectivity and enabling broadband emission collimation. This design provides a critical pathway to practical Si-integrated light-emitting systems.

2. RESULTS AND DISCUSSION

In our previous work, the radiation properties of a Si nanopillar placed on a SiO_2/Au heterostructure were investigated experimentally [12]. As schematically shown in Fig. 1(a), the hot electron luminescence from an isolated Si nanopillar on the heterostructure lacks good radiation directivity. Figure 1(b) shows the scanning electron microscopy (SEM) image of a single Si nanopillar. Under the resonant excitation of femtosecond laser pulses, the Si nanopillar emitted bright broadband PL, which was captured by a charge-coupled device (CCD) as displayed by the inset in Fig. 1(b). The starburst-shaped intensity profile implies substantial angular spreading in the light emissions.

To regulate the light emission direction, we position the Si nanopillar at the center of a circular Bragg grating that is composed of concentric Si rings, as illustrated in Fig. 1(c).

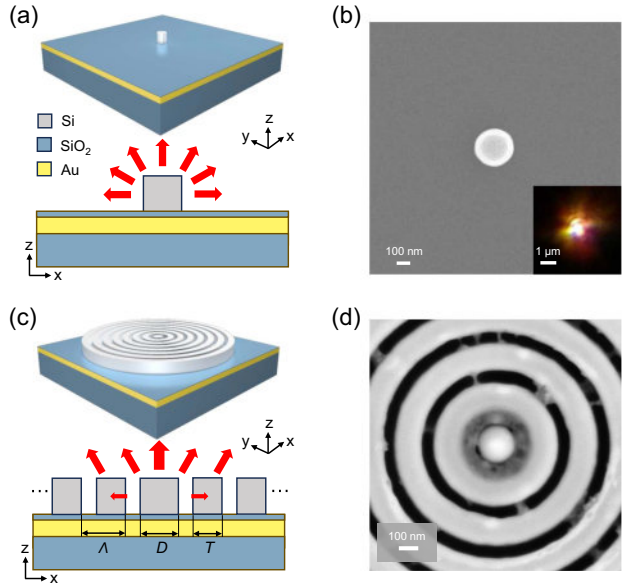

Fig. 1. (a) Schematic showing the structures and the radiative properties of a single Si nanopillar placed on a SiO_2/Au heterostructure. (b) Top-view SEM image of a single Si nanopillar. Its PL image captured by a CCD is shown in the inset. (c) Schematic showing the structures and the radiative properties of a bullseye resonator. (d) Top-view SEM image of a bullseye resonator.

The Au layer, with a thickness of approximately 100 nm, is employed to eliminate optical transmission while supporting SPP modes. A 15-nm-thick SiO_2 spacer layer is introduced to separate the Si bullseye resonator and the Au film, which is used to avoid the quenching of emission. The 220-nm-thick bullseye structure is patterned on the top layer through etching of a monocrystalline Si film. The central nanopillar acts as the light source, and the surrounding concentric rings serve as a resonant cavity. To allow sufficient tolerance for adjusting the central nanopillar's diameter, we set the inner diameter of the first concentric ring to 400 nm. The other key geometrical parameters are denoted as Λ (grating pitch), D (center nanopillar diameter), and T (ridge width). Figure 1(d) presents an SEM image of a fabricated bullseye resonator, demonstrating well-defined structural features. Detailed fabrication procedures are provided in Appendix A.

First, we performed finite-difference time-domain (FDTD) simulations by using a commercial software, Lumerical, to compare optical field enhancement under tight-focusing excitation conditions in both standalone Si nanopillars and bullseye resonators. As illustrated in Fig. 2(a), an x-polarized beam is focused through a 1.3 NA oil-immersion objective onto the central Si nanopillar. The field enhancement factor inside the Si nanopillar is defined as $\int_{Si}|E|^2 dV/(I_0 V_0)$, where V_0 is the volume of the nanopillar and I_0 represents the average light intensity over a 200-nm-diameter circular region centered on the incidence focal spot. In simulation, Λ and T were set as 190 and 140 nm, respectively. The calculated field enhancement spectra for different nanopillar diameters (D) are illustrated in Fig. 2(b). For a single nanopillar, the resonant wavelength red-shifts as its diameter increases; however, the optical field enhancement factor remains around 10. This indicates that increasing the diameter of a single nanopillar does not effectively enhance the localized field intensity within it.

When we analyze a bullseye resonator, the field enhancement factor in the central nanopillar is modulated by the surrounding circular Bragg grating. Since a portion of the excitation energy propagates outward via SPP modes, the enhanced backscattering of SPPs at specific wavelengths by the Bragg grating effectively suppresses lateral radiation from the bullseye center. This significantly improves the concentration of excitation energy at the central nanopillar. Conversely, when the target wavelength detunes from this condition, field enhancement becomes significantly suppressed. As shown in the lower panel of Fig. 2(b), for bullseye resonators with $D = 160$, 170, and 180 nm, the maximum field enhancement factors reach 16.2, 18.6, and 18.4, respectively. Since interband transitions in Si excited by photons in the wavelength range from 700 to 800 nm are dominated by 2PA and 3PA, the corresponding field enhancement of $|E|^4$ and $|E|^6$ provided by the bullseye structure must be considered. Taking the case of $D = 170$ nm as an example, the $|E|^4$ and $|E|^6$ enhancement factors reach 346 and 6436, respectively. These values are approximately 2.4 times and 3.7 times greater than those achieved with a single Si nanopillar, clearly demonstrating the important role of the bullseye structure in enhancing photoluminescence excitation efficiency in Si. These values represent significant improvements over those of the single Si nanopillar cases. Backscattering spectra calculations of the one-dimensional Bragg grating interacting with SPP modes reveal a broad backscattering peak near 746 nm (see Fig. 7 in Appendix B), which enhances the field confinement capability of the bullseye resonators within this spectral band. In addition, when the wavelength decreases below 700 nm, the grating-induced backscattering is significantly weakened. At the same time, the high-index rings enhance the waveguide effect in the SiO_2 spacer layer above the gold film, causing a portion of the resonant energy to be coupled into the waveguide modes of the SiO_2

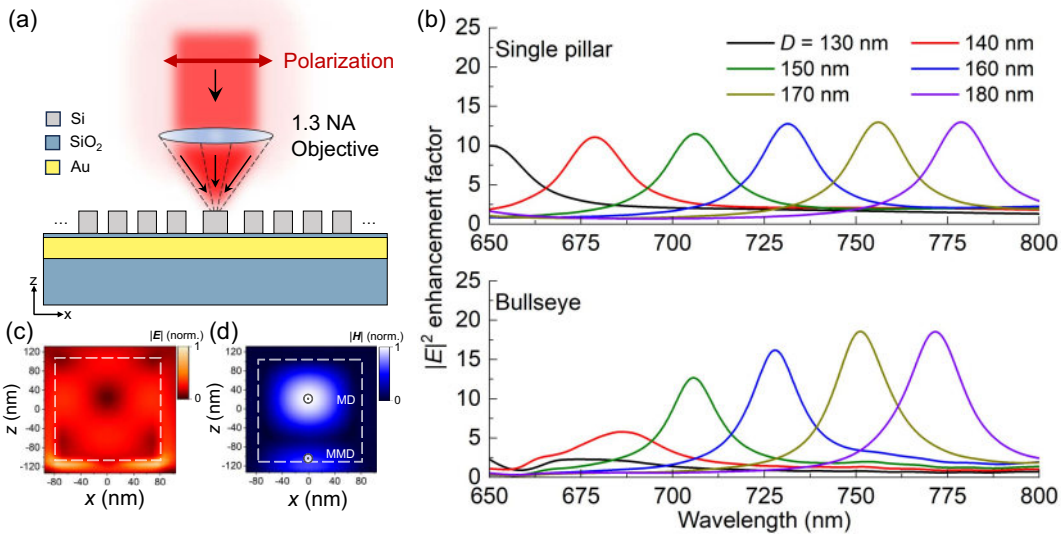

Fig. 2. Simulated optical response under focused linearly polarized excitation. (a) Schematic of focused illumination via a 1.3 NA oil-immersion objective on the bullseye resonator. (b) Calculated intensity ($|E|^2$) enhancement spectra in the single Si nanopillars (upper panel) and the central Si nanopillar of the bullseye resonators with different D (lower panel). (c) Electric field distribution and (d) magnetic field distribution of the central Si nanopillar ($D = 160$ nm) in the x–z plane at the wavelength of $\lambda = 728$ nm. The Si nanopillar is marked by white dashed lines.

spacer. As a result, the optical field in the central Si nanopillar is dramatically weakened. Figures 2(c) and 2(d) show the electric and magnetic field distributions, respectively, in the central region of a bullseye resonator with $D = 160$ nm at the resonant wavelength of 728 nm. It is shown that the resonance is hybridized from an MD localized in the upper segment of the nanopillar and an MMD confined to the nanopillar base.

Then, we discuss the PL intensity generated by a bullseye resonator with a central nanopillar of approximately 160 nm diameter under femtosecond laser excitation at different wavelengths. The actual structural parameters of the bullseye resonator we used agree with the designed values (see Fig. 6 in Appendix A). In the experiment, we tuned the center wavelength of the femtosecond laser from 710 to 740 nm in 2 nm steps while maintaining a laser power of 1 mW. The excitation light was focused onto the sample center through a 1.3 NA oil-immersion objective, with PL signals collected by a spectrometer (see detailed setup in Appendix C). The total PL intensity from the bullseye resonator was obtained by integrating the intensity throughout the spectrum from 400 to 613 nm. As indicated by the blue squares in Fig. 3(a), the measured peak value occurs at 726 nm. For comparison, the calculated electric field enhancement factor is also plotted in Fig. 3(a). It is demonstrated that the field enhancement peak aligns well with the measured highest PL intensity. Since the direct bandgap of Si is about 3.4 eV, 2PA dominates interband electron transition when the wavelength is smaller than 730 nm (1.7 eV); otherwise, only the 3PA process is allowed. Note that when the excitation wavelength shifts to shorter wavelengths away from the resonant peak, the PL intensity exhibits a sharp decline followed by a gradual increase. This occurs because the increased photon energy enhances the probability of stimulated electron transitions under nonresonant excitation.

In Fig. 3(b), we show the power-dependent PL of bullseye resonators with different diameters of the center nanopillar. The excitation wavelength was chosen at 726 nm, which is optimized for the sample with $D = 160$ nm. Consequently, a significant increase in PL intensity occurs when the excitation power exceeds 1 mW. However, for samples with $D = 140$ and 180 nm, off-resonant excitation requires threshold powers of 3 and 2.5 mW, respectively, to induce substantial PL emission. For the $D = 120$ and 200 nm samples, where the resonant wavelength lies farther from the excitation wavelength, significant PL enhancement remains difficult to achieve even at 5.5 mW excitation power. Therefore, the results reveal the importance of resonant enhancement at the excitation stage.

Next, we examine the emission characteristics of bullseye resonators. Figure 4(a) displays the emission spectra under different excitation powers, alongside the corresponding CCD-captured PL images. A broad emission peak around 580 nm was observed, resulting in the yellow–green emission spot shown in the insets. Spectra acquired at 1 and 5 mW excitation powers are presented at the bottom and top of Fig. 4(a), respectively. The strongest emission peak appears at the wavelength of ~577 nm, as indicated by the white dashed line. Gaussian fitting reveals that the spectrum consists of six emission peaks with intensity ratios minimally sensitive to excitation power.

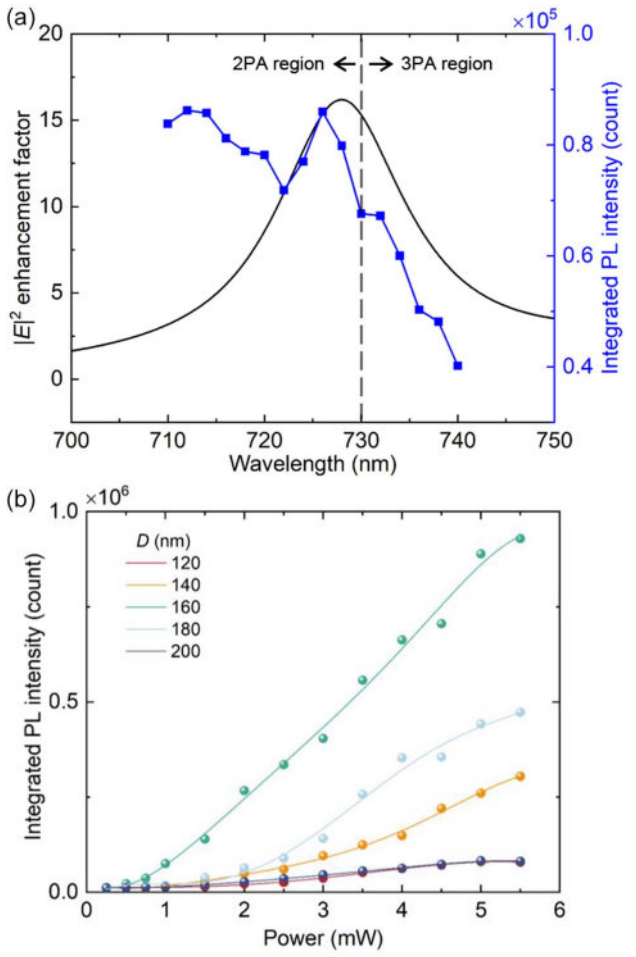

Fig. 3. (a) For a bullseye resonator with $D = 160$ nm, the dependence of the integrated PL intensity on the excitation wavelength is indicated by blue squares; the black curve shows the calculated optical field enhancement factor for comparison. (b) Power-dependent PL intensity under the excitation of a 726-nm femtosecond laser for bullseye resonators with different center nanopillar diameters.

Then, we need to elucidate the formation mechanism of the emission spectra. In general, the photon-generated hot electron distribution is consistent with the electric field distribution after the excitation of femtosecond laser pulses [28,29]. Thus, the emission from the bullseye is equivalent to the overlapped radiation of an MD and an MMD [see Fig. 2(d)] at the center of the circular Bragg grating. The setting of the simulation model is shown schematically in the inset of Fig. 4(b), in which the two MD light sources were placed above the SiO_2 spacer surface with height positions of 130 and 10 nm, respectively. The calculated emission peaks indicated by a black curve agree with the measured result (under 2 mW excitation) shown by a blue curve. The only difference is that the experimentally emitted energy concentrates at dual peaks of 577 and 589 nm. This phenomenon primarily stems from mode competition, meaning that under a fixed total emission energy, enhanced emission in certain wavelength bands to attenuation in others. The simulation results indicate that the emission efficiency is higher in the 550–600 nm range. Therefore, the majority of the

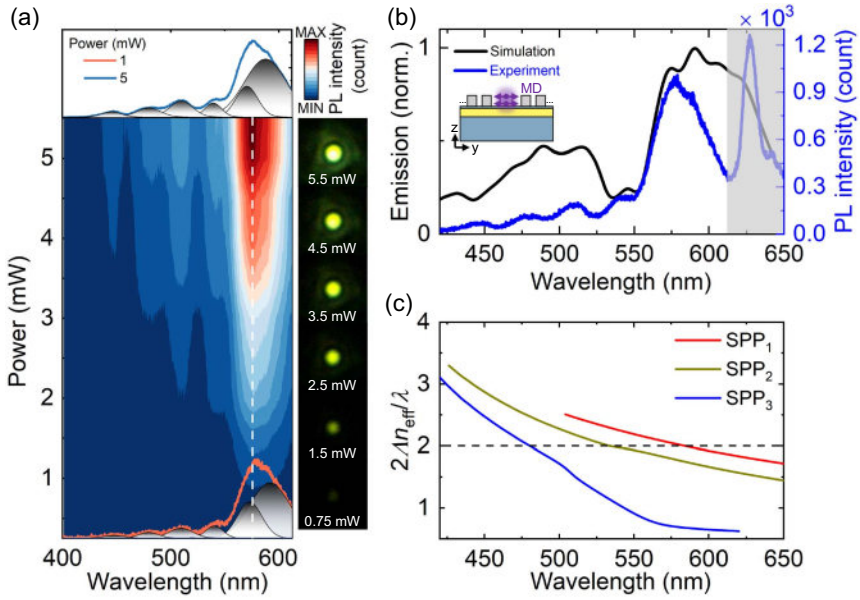

Fig. 4. (a) Measured PL spectra of the bullseye resonator ($D = 160$ nm) with increasing laser power. The spectra of $P = 1$ and 5 mW are shown as insets. The black curves represent the Gaussian multipeak fitting of the spectra. Also shown are the corresponding emission images captured by a CCD. (b) Comparison of the calculated emission spectrum (black curve) with the measured PL spectrum under 2 mW excitation (blue curve). The gray shade marks the cutting region of the dichroic mirror. The simulation model is shown as an inset, where the central Si nanopillar is replaced by two magnetic dipole sources oriented along the y axis. (c) Calculated Bragg condition of the SPP modes as a function of wavelength.

energy is emitted within this band in experiments. However, the emission spectrum obtained from simulation is normalized based on the source power spectrum (on the order of 10^{-15} W), thereby eliminating the influence of variations in source power with wavelength. The shaded region (613–650 nm) in the figure corresponds to the transmission band edge of the dichroic mirror, which contains signal spikes originating from dramatic changes in interference behavior [30] and should be discarded as invalid data.

In Fig. 4(c), we calculated the orders of the Bragg condition, expressed as $2\Lambda n_{\text{eff}}/\lambda$, for three distinct SPP modes over the whole emission wavelength band. Here n_{eff} is the model effective index for SPP modes, and λ is the free-space wavelength. The parameter n_{eff} was computed using a weighted average of the effective refractive indices governing SPP propagation through air gaps and Si grating regions [31]. The emergence of higher-order modes within the Si gratings necessitates solving for three distinct SPP effective indices (see Fig. 8 in Appendix B), which are noted as SPP_{1-3} in Fig. 4(c). It is found that emission peaks align with the second-order Bragg condition of the three SPP modes around wavelengths of 584, 535, and 480 nm. According to the momentum matching relation at the second-order Bragg condition, the efficient out-coupling direction is expected to be perpendicular to the plane of the grating [32–35]. It indicates that most of the radiative power from the bullseye resonator could be collected by a small-NA objective.

In the following, we measured the PL spectra of the bullseye resonator ($D = 160$ nm) by using an NA-variable oil-immersion objective (NA = 0.7–1.3); the results are shown in Fig. 5(a). The PL intensity spectra collected using 1.3 NA and 0.7 NA objectives are represented by the red and blue lines, respectively. Data in the shaded region of the graph are disregarded. It can be observed that varying the collection half-aperture angle has little effect on either the spectral profile or intensity of the emission. To corroborate the experimental measurements, we computed the emission spectra of the bullseye resonator by integrating over the far field within different half-aperture angles (α varies from 10° to 64°) as shown in Fig. 5(b). According to the relationship $\text{NA} = n_{\text{oil}} \cdot \sin\alpha$, where $n_{\text{oil}} = 1.45$, an NA of 0.7 corresponds to a half-aperture angle of 29°, while an NA of 1.3 corresponds to 64°. As shown in Fig. 5(b), when the far-field half-aperture angle increases from 10° to 29°, the received emission intensity grows significantly with the angle. However, as the half-aperture angle exceeds 29°, the growth in emission intensity with respect to the receiving angle slows noticeably, approaching saturation at 50°. Therefore, in theory, all the emitted energy can be collected within a half-aperture angle of 64°.

To further demonstrate the contribution of the bullseye structure to emission directivity, the upper panel of Fig. 5(c) compares the proportion of total emitted energy collected within different aperture angles for the two magnetic dipole sources, with and without the bullseye structure. It can be observed that the bullseye structure yields a much higher proportion of received energy at half-aperture angles ≤40° compared to the case without it. Specifically, the bullseye structure concentrates nearly 80% of the emitted energy within a 30° half-aperture angle, a value 2.6 times higher than the case without the structure. This highlights the role of the bullseye in directing the hot electron luminescence from the central Si nanopillar. The lower panel of Fig. 5(c) shows the PL collection

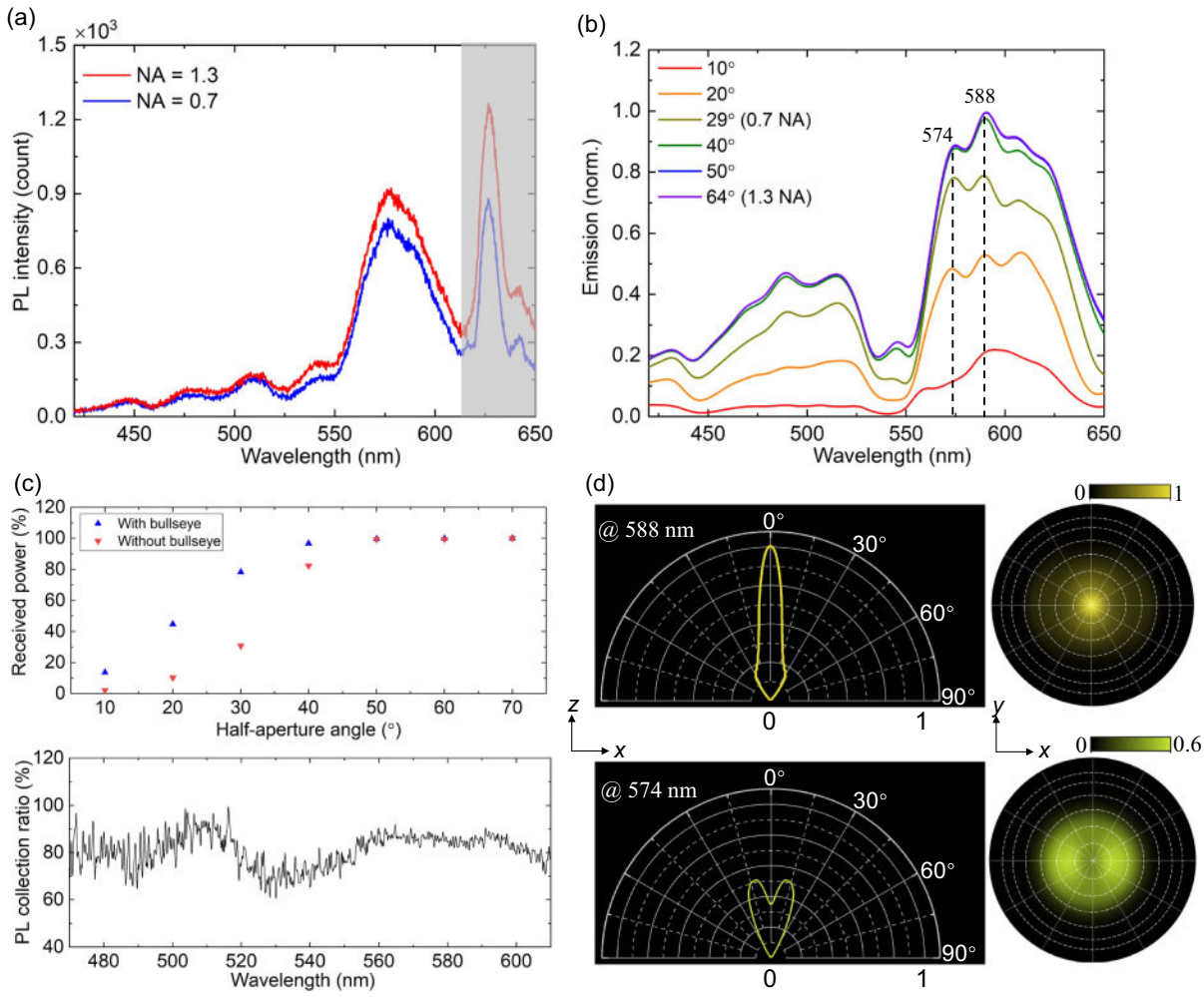

Fig. 5. (a) PL spectra collected by objectives with 1.3 NA (red) and 0.7 NA (blue). A gray shade marks the cutting region of the dichroic mirror. (b) Emission spectra calculated within different far-field collection angles (normalized to the total emission spectrum over the upper hemisphere), where the 29° and 64° half-aperture angles correspond to the conditions of using a 0.7 NA and a 1.3 NA oil-immersion objective, respectively. (c) The upper panel is the calculated power of the whole emission spectra (from 420 to 650 nm) within different aperture angles with bullseye resonator (blue) and without bullseye resonator (red); the values are normalized to the total power emitted into the upper hemisphere. The lower panel is the PL collection ratio obtained by dividing the measured 0.7 NA spectrum by the 1.3 NA spectrum. (d) Far-field radiative patterns of the typical emission peaks at the wavelengths of 588 (upper panel) and 574 nm (lower panel). The solid line shows the emission intensity along various polar angle directions in the x–z plane, while the contour map represents the intensity distribution on the upper radiating hemisphere.

ratio, obtained by dividing the 0.7 NA spectrum by the 1.3 NA spectrum. Across the emission range of 470–600 nm, the collection ratio remains above 60%. Notably, within the 570–590 nm spectral region covering the main emission peak, the ratio remains at approximately 85%. This demonstrates that the designed bullseye resonator exhibits good vertical emission characteristics.

Figure 5(d) presents the far-field patterns of emission peaks at wavelengths of 588 nm (upper panel) and 574 nm (lower panel). It can be seen that all radiation is collected by the 1.3 NA (64°) objective, with the primary emission concentrated within a 29° (0.7 NA) half-aperture angle. For the 588 nm emission mode, energy is primarily emitted perpendicular to the bullseye resonator (in the 0° direction), demonstrating excellent directional characteristics. In addition, the 574 nm emission mode exhibits a doughnut-shaped far-field radiation pattern, with a peak emission half-angle of 10°. These simulation results further confirm that the designed bullseye resonator exhibits good directional emission characteristics within a 29° half-aperture angle.

3. CONCLUSION

In summary, we have designed and fabricated Si bullseye resonators on a SiO_2/Au substrate, which is compatible with standard nano-fabrication techniques, demonstrating their capability for broadband directional enhanced hot electron luminescence. The central Si nanopillar enhances excitation efficiency via MD and MMD modes under the femtosecond-laser-driven 2PA. In the meantime, based on the second-order Bragg condition, the gratings efficiently out-couple propagating SPP modes into distinct spectral peaks, generating enhanced emission. Experimental validation confirms that a 0.7 NA

objective collects more than 60% of emitted energy across the 470–600 nm wavelength band. Importantly, within the 570–590 nm spectral region covering the main emission peak, the collection efficiency remains at approximately 85%. This architecture uniquely provides concurrent enhancement of Si photoluminescence at both excitation (resonance-driven) and emission (grating-collimated) stages, offering a practical pathway toward realizing efficient, directive, mode-selective light sources for silicon-integrated photonics.

APPENDIX A: SAMPLE FABRICATION

In this work, we transferred the thin monocrystalline Si film of a silicon-on-insulator (SOI) wafer to a quartz substrate by using the combination of adhesive wafer bonding and chemical polishing [see Fig. 6(a)]. First, a 100-nm-thick Au film and a 15-nm-thick SiO_2 film were deposited sequentially on an SOI wafer comprising a 220-nm-thick Si film on a 2-μm-thick SiO_2 substrate. Then, an ultraviolet (UV) light curable adhesive (NOA61) was spin-coated on the sample, followed by bonding to the quartz substrate. After that, the sample was illuminated by using 365-nm UV light to cross-link the adhesive for 4 h. In order to achieve optimum adhesion, the sample was baked beforehand at 50°C for 1 day. The Si substrate was then removed by chemical polishing and dry etching. Finally, the c-Si on quartz substrate was obtained by removing the SiO_2 substrate of the SOI wafer with hydrofluoric (HF) acid.

Patterning of bullseye resonators was realized by using the combination of electron-beam exposure of positive resist and dry etching. The sample was first spin-coated with a 400-nm-thick resist for electron beam (ARP6200.09). Then, the pattern was exposed by using an electron-beam lithography system (EBPG5000Plus, Raith) operated at 100 kV. After that, the resist was developed with xylene, and the pattern transfer was realized by using an inductively coupled plasma tool (Plasmalab System 100 ICP 180, Oxford Instruments). Lastly, to eliminate the nonradiative recombination centers induced in the fabrication process, the fabricated bullseye resonators were covered with a 5-nm-thick Al_2O_3 layer by using an atomic layer deposition system (SUNALE R-150, Picosun). The morphologies of bullseye resonators were characterized by using scanning electron microscopy (Ultra 55, Zeiss), as shown in Figs. 6(b) and 6(c).

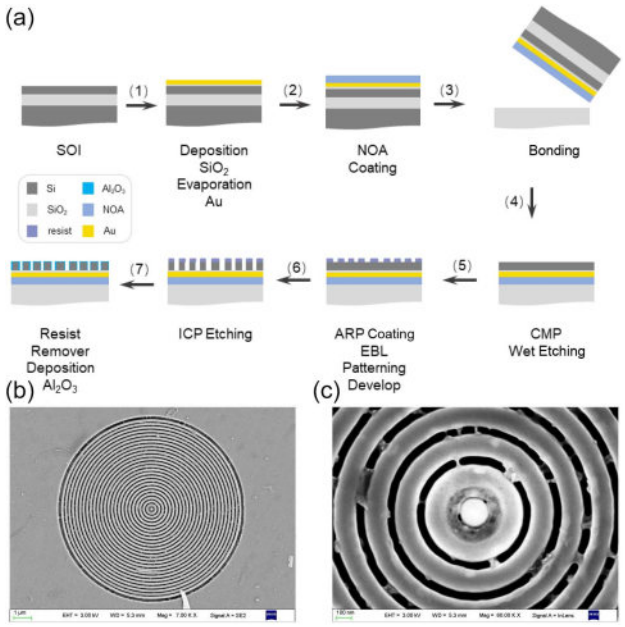

Fig. 6. (a) Procedure for fabricating bullseye resonators on a SiO_2/Au substrate. (b) Top view of the whole bullseye resonator ($D = 160$ nm). (c) Magnified view of the bullseye's central area ($D = 160$ nm).

APPENDIX B: NUMERICAL SIMULATION

The field enhancement and emission spectra were calculated by using the FDTD method based on the commercial software Lumerical. The entire simulation model contains 24 grating periods. A perfectly matched boundary condition was employed to terminate the simulation region. The refractive indices of dielectric materials and Au were taken from Ref. [36] and the *CRC Handbook of Chemistry and Physics* [37], respectively. A monitor covering the entire sample area is positioned 460 nm above the bullseye to record the emission spectrum. The emission source is equivalently simulated as two equal-intensity y-oriented MD light sources located at the center of the circular Bragg grating. Their heights above the SiO_2 substrate are 130 and 10 nm, respectively. The far-field emission was calculated by using a near-to-far field transformation based on the field distributions obtained by the monitor.

The simulations for SPP modes were conducted in COMSOL Multiphysics employing the finite element method. The bullseye resonator is simplified as a one-dimensional Bragg grating with periodic modulation along the x axis. This model allows us to investigate its backscattering effects on SPP modes propagating laterally. The model incorporated a 20-unit-cell Bragg grating structure with geometric parameters matching the bullseye resonator's concentric rings. Perfectly matched layers bounded the computational domain to suppress boundary reflections. Excitation was achieved via boundary mode analysis, launching an SPP wave propagating rightward from a port offset 200 nm from the edge of the first grating unit. The backscattering ratio is defined as $|\int_{\text{port}}(E_c - E_{\text{spp}} \cdot E_{\text{spp}}^*)\mathrm{d}A / \int_{\text{port}}(E_{\text{spp}} \cdot E_{\text{spp}}^*)\mathrm{d}A|^2$, where E_{spp} is the input SPP field and E_c is the computed electric field on the port consisting of the SPP field and the backscattered field. Figure 7(a) shows the backscattering spectrum of the SPP produced by the Bragg grating. Starting from 650 nm, the backscattering ratio increases with wavelength, reaching its maximum at 746 nm. Subsequently, it exhibits an oscillatory decline as the wavelength continues to grow. This trend aligns with the variation of the maximum field enhancement factor in the bullseye structure shown in Fig. 2(b) of the main text. These results demonstrate that the backscattering enhancement induced by the Bragg grating can strengthen the optical field localization capability at the center of the bullseye resonator. Figures 7(b)–7(d) illustrate the electric field amplitude distributions at three characteristic wavelengths: 728, 746, and 770 nm, respectively. At 746 nm, the electric field primarily exists as SPP modes, with significantly weaker radiation in the obliquely upward direction compared to those in the cases of 728 and 770 nm.

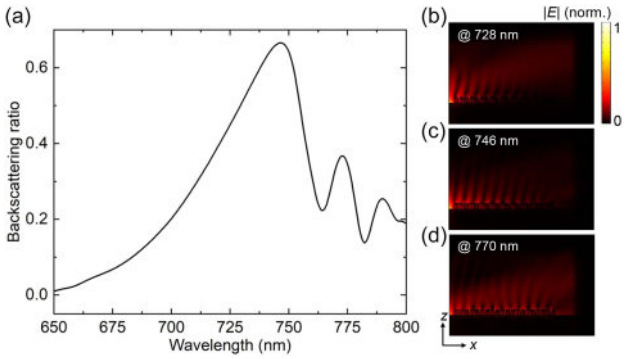

Fig. 7. (a) Simulated backscattering spectrum of an SPP mode in the Bragg grating. (b)–(d) illustrate the spatial distribution of electric field amplitude after interaction between the SPP mode and Bragg grating at the wavelengths of 728, 746, and 770 nm, respectively.

The effective refractive indices (n_{eff}) of SPP modes were calculated using the boundary mode analysis module in COMSOL Multiphysics. Within the grating gap regions, only one SPP eigenmode exists, with its out-of-plane electric field component (E_z) distribution shown in Fig. 8(a). However, three distinct SPP eigenmodes emerge inside the Si grating ridges, ordered by descending n_{eff} values. Their corresponding E_z distributions are presented in Figs. 8(b)–8(d). When interacting with the grating structure, the average n_{eff} experienced by SPPs is governed by the following expression [31]:

$$n_{\text{eff}} = n_{\text{eff}}^{(0)}\left(\frac{\Lambda - T}{\Lambda}\right) + n_{\text{eff}}^{(i)}\left(\frac{T}{\Lambda}\right) \quad (i = 1,2,3),$$

where $n_{\text{eff}}^{(0)}$ represents the effective index of the SPP mode in the air gap region, and $n_{\text{eff}}^{(i)}$ represents the effective index of the SPP modes in the Si grating ridges.

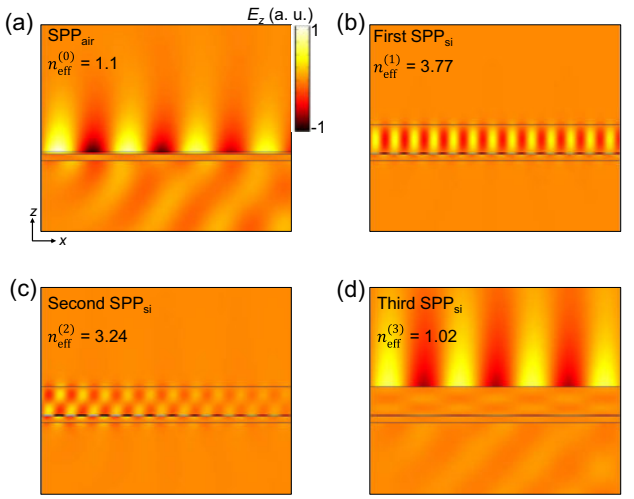

Fig. 8. Model profiles and effective indices of SPP modes at the wavelength of 588 nm. (a) Results of the SPP mode in the air gap region. (b)–(d) Results of three SPP modes in the Si grating ridges, respectively.

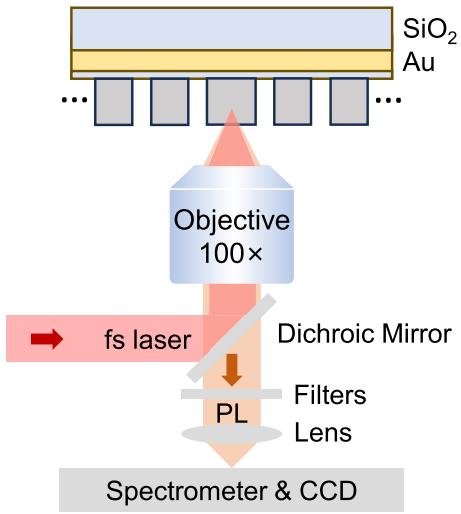

Fig. 9. Experimental setups used to characterize the nonlinear optical responses of Si bullseye resonator.

APPENDIX C: OPTICAL CHARACTERIZATION

The optical properties of the bullseye resonator were characterized by using an inverted microscope (Observer A1, Zeiss) equipped with white light and femtosecond laser light as excitation sources. The system is shown schematically in Fig. 9. For the characterization of nonlinear optical responses, we used 726-nm femtosecond laser pulses with a duration of 130 fs and a repetition rate of 76 MHz (Mira HP, Coherent) to excite the Si bullseye. The excitation light was focused on Si bullseye resonators by using a 100 × NA-variable oil-immersion objective (NA = 0.7–1.3) of the microscope (refractive index of the oil $n_{\text{oil}} = 1.45$), and the hot electron luminescence emitted from Si bullseye resonators was collected by using the same objective and directed to a spectrometer (SR-500i-B1, Andor) for spectral analysis or to a charge-coupled device (DU970N, Andor) for imaging.

Funding. National Natural Science Foundation of China (12174123, 12374347); Guangzhou Municipal Science and Technology Bureau (SL2024A04J00197); Scientific Research Innovation Project of Graduate School of South China Normal University.

Disclosures. The authors declare no conflicts of interest.

Data Availability. Data underlying the results presented in this paper are not publicly available at this time but may be obtained from the authors upon reasonable request.

REFERENCES

1. L. Pavesi, L. Dal Negro, C. Mazzoleni, *et al.*, "Optical gain in silicon nanocrystals," Nature **408**, 440–444 (2000).
2. L. Pavesi, "Silicon-based light sources for silicon integrated circuits," Adv. Opt. Technol. **2008**, 416926 (2008).
3. A. I. Kuznetsov, A. E. Miroshnichenko, M. L. Brongersma, *et al.*, "Optically resonant dielectric nanostructures," Science **354**, aag2472 (2016).
4. Y. Kivshar, "The rise of Mie-tronics," Nano Lett. **22**, 3513–3515 (2022).

5. M. Panmai and S. Lan, "Rising tide of enhanced crystalline silicon luminescence via optical resonance," Nano Lett. **24**, 14091–14094 (2024).
6. M. Panmai, J. Xiang, S. Li, *et al.*, "Highly efficient nonlinear optical emission from a subwavelength crystalline silicon cuboid mediated by supercavity mode," Nat. Commun. **13**, 2749 (2022).
7. C. Zhang, Y. Xu, J. Liu, *et al.*, "Lighting up silicon nanoparticles with Mie resonances," Nat. Commun. **9**, 2964 (2018).
8. T. Peng, Z. Wang, S. Li, *et al.*, "Si/Si_3N_4/Ag hybrid nanocavity: a platform for enhancing light-matter interaction," Photonics Res. **13**, 709–720 (2025).
9. Y. Mao, S. Bai, M. Panmai, *et al.*, "Controllable shaping of high-index dielectric nanoparticles by exploiting the giant optical force of femtosecond laser pulses," Photonics Res. **12**, 282–291 (2024).
10. M. V. Rybin, K. L. Koshelev, Z. F. Sadrieva, *et al.*, "High-*Q* supercavity modes in subwavelength dielectric resonators," Phys. Rev. Lett. **119**, 243901 (2017).
11. J. Xiang, Y. Xu, J.-D. Chen, *et al.*, "Tailoring the spatial localization of bound state in the continuum in plasmonic-dielectric hybrid system," Nanophotonics **9**, 133–142 (2020).
12. L. Zhou, M. Panmai, S. Li, *et al.*, "Lighting up Si nanoparticle arrays by exploiting the bound states in the continuum formed in a Si/Au hybrid nanostructure," ACS Photonics **9**, 2991–2999 (2022).
13. Y. Liang, K. Koshelev, F. Zhang, *et al.*, "Bound states in the continuum in anisotropic plasmonic metasurfaces," Nano Lett. **20**, 6351–6356 (2020).
14. Z. Wang, Y. Liang, J. Qu, *et al.*, "Plasmonic bound states in the continuum for unpolarized weak spatially coherent light," Photonics Res. **11**, 260–269 (2023).
15. J. Xiang, J. Chen, Q. Dai, *et al.*, "Modifying Mie resonances and carrier dynamics of silicon nanoparticles by dense electron-hole plasmas," Phys. Rev. Appl. **13**, 014003 (2020).
16. A. Liu, P. Wolf, J. A. Lott, *et al.*, "Vertical-cavity surface-emitting lasers for data communication and sensing," Photonics Res. **7**, 121–136 (2019).
17. W. Zhou and M. Pan, "The future of photonic crystal surface-emitting lasers," Appl. Phys. Lett. **123**, 140501 (2023).
18. X. Sun and A. Yariv, "Surface-emitting circular DFB, disk-, and ring-Bragg resonator lasers with chirped gratings: a unified theory and comparative study," Opt. Express **16**, 9155–9164 (2008).
19. G. Pan, M. Xun, X. Zhou, *et al.*, "Harnessing the capabilities of VCSELs: unlocking the potential for advanced integrated photonic devices and systems," Light Sci. Appl. **13**, 229 (2024).
20. G. Yang, Q. Shen, Y. Niu, *et al.*, "Unidirectional, ultrafast, and bright spontaneous emission source enabled by a hybrid plasmonic nanoantenna," Laser Photonics Rev. **14**, 1900213 (2020).
21. D. Komisar, S. Kumar, Y. Kan, *et al.*, "Generation of radially polarized single photons with plasmonic bullseye antennas," ACS Photonics **8**, 2190–2196 (2021).
22. K. S. Hong, H.-J. Lim, Y.-H. Ko, *et al.*, "Boosting single-photon extraction efficiency in GaN through radiative mode conversion," Laser Photonics Rev. **19**, 2401966 (2025).
23. J.-M. Yi, V. Smirnov, X. Piao, *et al.*, "Suppression of radiative damping and enhancement of second harmonic generation in bull's eye nanoresonators," ACS Nano **10**, 475–483 (2016).
24. Z. Li, Z. Hu, X. Ye, *et al.*, "Enhanced second-harmonic generation in thin-film lithium niobate circular Bragg nanocavity," Nano Lett. **24**, 11676–11682 (2024).
25. A. B. Evlyukhin, S. M. Novikov, U. Zywietz, *et al.*, "Demonstration of magnetic dipole resonances of dielectric nanospheres in the visible region," Nano Lett. **12**, 3749–3755 (2012).
26. L. Shi, E. Xifré-Pérez, F. J. García de Abajo, *et al.*, "Looking through the mirror: optical microcavity-mirror image photonic interaction," Opt. Express **20**, 11247–11255 (2012).
27. E. Xifré-Pérez, L. Shi, U. Tuzer, *et al.*, "Mirror-image-induced magnetic modes," ACS Nano **7**, 664–668 (2013).
28. A. Rudenko, K. Ladutenko, S. Makarov, *et al.*, "Photogenerated free carrier-induced symmetry breaking in spherical silicon nanoparticle," Adv. Opt. Mater. **6**, 1701153 (2018).
29. G. Crotti, A. Schirato, O. Pashina, *et al.*, "Ultrafast switching of a metasurface quasi-bound state in the continuum via transient optical symmetry breaking," Light Sci. Appl. **14**, 240 (2025).
30. Q. Zhang, Q. Jin, A. Mertens, *et al.*, "Fabrication of Bragg mirrors by multilayer Inkjet printing," Adv. Mater. **34**, 2201348 (2022).
31. Y. Kan, S. K. H. Andersen, F. Ding, *et al.*, "Metasurface-enabled generation of circularly polarized single photons," Adv. Mater. **32**, 1907832 (2020).
32. G. Maisons, M. Carras, M. Garcia, *et al.*, "Directional single mode quantum cascade laser emission using second-order metal grating coupler," Appl. Phys. Lett. **98**, 021101 (2011).
33. M. Davanço, M. T. Rakher, D. Schuh, *et al.*, "A circular dielectric grating for vertical extraction of single quantum dot emission," Appl. Phys. Lett. **99**, 041102 (2011).
34. J. Liu, R. Su, Y. Wei, *et al.*, "A solid-state source of strongly entangled photon pairs with high brightness and indistinguishability," Nat. Nanotechnol. **14**, 586–593 (2019).
35. L. Li, E. H. Chen, J. Zheng, *et al.*, "Efficient photon collection from a nitrogen vacancy center in a circular bullseye grating," Nano Lett. **15**, 1493–1497 (2015).
36. E. D. Palik, "Handbook of optical constants of solids," in *Handbook of Optical Constants of Solids* (Academic Press, 1997).
37. W. M. Haynes, *CRC Handbook of Chemistry and Physics* (CRC Press, 2016).